Title

The Role of Roughening to Enhance Selectivity to C2+ Products during CO2 Electroreduction on Copper

Journal

ACS Energy Letters, 6(9)

ISSN

2380-8195

Authors

Gauthier, Joseph A
Stenlid, Joakim Halldin
Abild-Pedersen, Frank
et al.

Publication Date

2021-09-10

DOI

10.1021/acsenergylett.1c01485

Peer reviewed

ACS Energy LETTERS

http://pubs.acs.org/journal/aelccp

LETTER

The Role of Roughening to Enhance Selectivity to C_{2+} Products during CO_2 Electroreduction on Copper

Joseph A. Gauthier,[⊥] Joakim Halldin Stenlid,[⊥] Frank Abild-Pedersen,* Martin Head-Gordon,* and Alexis T. Bell*

Cite This: *ACS Energy Lett.* 2021, 6, 3252−3260

Read Online

ACCESS | Metrics & More | Article Recommendations | Supporting Information

ABSTRACT: Roughened copper electrodes, including those derived from cuprous oxide, have long been known to exhibit an enhanced Faradaic efficiency to C_{2+} products during CO_2 electroreduction. However, the source of this enhancement has not been rationalized mechanistically. In this work, we present a theoretical study of roughened copper electrodes derived from cuprous oxide, phosphide, nitride, and sulfide. We utilize a carefully benchmarked effective medium theory potential to develop geometric models of the roughened electrodes on an unprecedented scale. Using density functional theory with an implicit electrolyte, we determine applied bias dependent binding energy distributions for critical reaction intermediates. We apply simple thermodynamic models to evaluate the role of surface roughening on selectivity during CO_2 electroreduction. We find that the manner of roughening (i.e., starting from oxide, phosphide, sulfide, or nitride) does not significantly affect the binding energy distributions found, and we suggest design rules to maximize selectivity to C_{2+} products on copper.

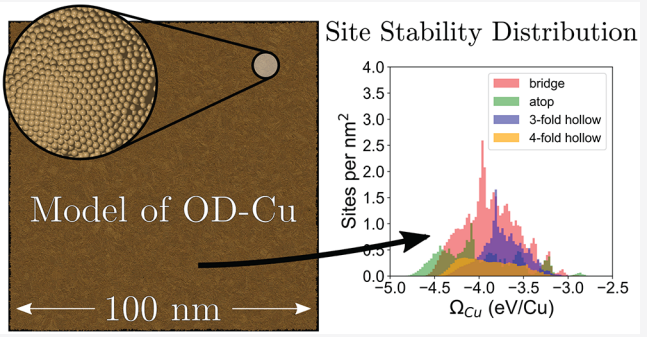

Electroreduction of CO_2 (CO2RR) and CO is emerging as a promising route to sustainably produce fuels and important commodity chemicals such as ethylene and ethanol and also as a path to mitigate point sources of CO_2, a potent greenhouse gas, in an economically attractive way.[1] Despite decades of research efforts, Cu remains the only catalyst capable of producing significant amounts of C_{2+} products, containing more than one carbon atom.[2] In doing so, however, Cu also produces a medley of other products of varying economic value, presenting a challenge for industrial viability in the absence of a carbon tax or credit.[3,4] Several strategies for improving the Faradaic efficiency of Cu toward C_{2+} products have emerged, including engineering of the electrode assembly[5−11] and electrolyte,[12−15] dynamic potential control,[16−18] and surface roughening.[19−24] In this contribution, we examine opportunities and intrinsic limitations in tuning catalytic selectivity of copper via surface structure engineering.

CO_2 reduction on Cu has long been known to be quite sensitive to the precise surface structure, with early results from Hori illustrating variations in activity and selectivity on single crystal electrodes.[25,26] For well-characterized surfaces, enhancement in selectivity to C_{2+} products on undercoordinated facets has been rationalized by strengthened CO binding,[27,28] and in the case of facets containing square sites, enhanced C−C bond formation,[29,30] where transient atomic C on the surface has been proposed to play a key role.[31,32] However, the precise role of surface roughening in enhancing the Faradaic efficiency to C_{2+} products remains a point of debate, in particular for electrodes derived from cuprous oxide or nitride.[33−40] Disagreement in the literature over something as fundamental as the oxidation state of Cu during CO_2 reduction highlights the difficulty of probing the solid−liquid interface with spectroscopic approaches.

Quantum mechanical methods provide a path for probing the solid−liquid interface where modern experimental methods fail.[41,42] However, they suffer from exponential cost scaling that limits systems to those with near-perfect order, unlike the complex nanostructures found in actual electrode

Received: July 16, 2021
Accepted: August 18, 2021
Published: August 23, 2021

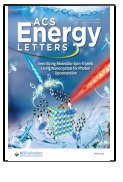

https://doi.org/10.1021/acsenergylett.1c01485
ACS Energy Lett. 2021, 6, 3252−3260

assemblies, particularly those with roughened electrode surfaces. Most commonly, surface roughness is approximated by investigating a small number of undercoordinated single crystal facets with density functional theory (DFT).[43−45] Such an approach neglects the more delicate morphology found in real electrodes, but can allow for generalized conclusions about the reaction mechanism. Previous efforts to deliberately incorporate surface roughness into computational models have relied on brute-force *ab initio* molecular dynamics simulations,[46] or have utilized neural network methods to predict simple intermediate binding energies[24] and simulate annealing of larger systems.[39,47]

Inspired by recent advancements in *operando* spectroscopy[34,48] and DFT calculations,[49,50] in this Letter we present a theoretical investigation into how surface roughening from "derived" Cu surfaces (reduced from an oxidized state) affects catalysis toward CO_2 reduction. We leverage a low-cost classical potential, effective medium theory (EMT),[51−53] efficiently implemented in the Asap3 package of the Atomic Simulation Environment.[54] We benchmarked EMT against semilocal DFT (see SI Note 2, Figures S1−S4) and generated structural models of roughened copper surfaces derived from cuprous oxide (OD-Cu), nitride, phosphide, and sulfide, with system sizes nearing the micron scale, containing between 8 and 15 million atoms. All surfaces had 80 layers of metal atoms which we found was enough to eliminate template matching effects on the surface (see SI Note 3, Figure S5). Our approach to generating structural models of derived Cu surfaces is illustrated in Figure 1. Although our structural models capture

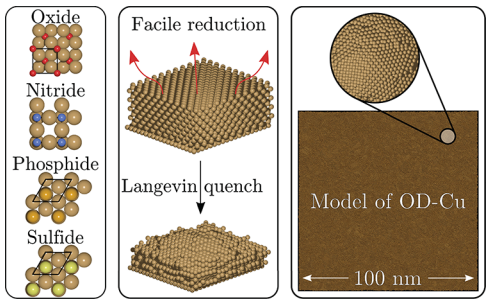

Figure 1. Illustration of our approach to modeling copper surfaces derived from cuprous oxide, nitride, phosphide, and sulfide. Starting from bulk structures, we produce surfaces of, for example, Cu_2O and assume facile reduction to metallic Cu based on recent *operando* spectroscopy[34,48] and DFT calculations.[49,50] Using EMT, we then quench the high energy surface with a short Langevin dynamics simulation before optimizing the geometry.

a wide range of surface morphologies not found in single crystal models, they lack the mesoscale structuring that is often observed in experimental electrodes.[24,55] The lack of mesoscale structuring results in a relatively low surface roughness factor, below 1.5.

Beginning with bulk cells for cuprous oxide, nitride, phosphide, and sulfide optimized with semilocal (RPBE) DFT[56] implemented in VASP,[57−59] we assumed facile reduction to metallic Cu based on recent *operando* spectroscopic evidence,[34,48] published DFT calculations,[49,50] and our own calculations (see SI Note 4, Figure S6). Although our calculations and *operando* spectroscopy suggest it is unlikely, the presence of any kinetically trapped residual oxide may affect the analysis presented in this work. Using EMT, we used this high energy structure, with the bottom two layers fixed to provide support, as a starting point for a Langevin dynamics simulation with a high friction coefficient to quench the surface while still preserving structure. We then optimized the geometry of the quenched surface until the maximum force on a nonfixed atom in the surface was below 0.05 eV $Å^{-1}$. Further details of the DFT employed in this study can be found in the Computational Details section of the SI.

For each structural model produced via EMT, we computed a distribution of Cu binding energies as a function of the applied bias using the α parameter scheme (see below) based on the local coordination environment,[60−63] summarized in Scheme 1. In this scheme, the constant potential copper

Scheme 1. Illustration of Our Approach to Computing Distributions of Cu Binding Energies Given the Structural Models Produced from EMT[a]

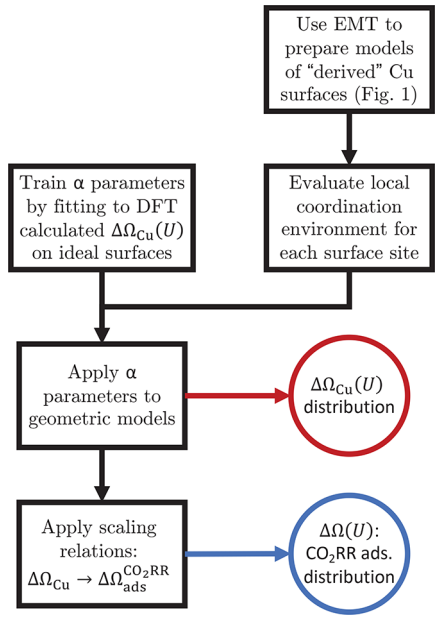

[a]Further details of the α parameter scheme can be found in the SI, or in references 60, 62, and 63.

binding energy ($\Delta\Omega_{Cu}$) is computed given only the local coordination environment as an input, with MAE less than 0.1 eV for Cu systems relative to semilocal DFT.[62,63]

For an fcc metal like Cu, with a 12-fold bulk coordination, there are 12 α parameters (α_{CN}) each representing the average atom-wise energy associated with the formation of a Cu−Cu bond leading to the coordination number CN. (For technical reasons, CN 1−3 are commonly grouped as one parameter, α_{1-3}.) The cohesive energy, or binding energy, of an atom is obtained as the sum over all the new bonds formed when placing the atom at a given environment (e.g., a surface site) from a gas phase reference, taking both the atom itself and its nearest neighbors into account. When considering a surface site containing more than one atom, the binding energy is computed from the total number of bonds formed, accounting for all atoms of the site as well as their neighbors. A more detailed description of the α parameters scheme is found in references 60, 62, and 63 and in SI Note 7.

The α parameters in our model were trained by computing $\Delta\Omega_{Cu}$ with DFT on several single crystal facets of varying coordination representing the main classes of expected site ensembles on the roughened copper surfaces, using the RPBE

https://doi.org/10.1021/acsenergylett.1c01485
ACS Energy Lett. 2021, 6, 3252−3260

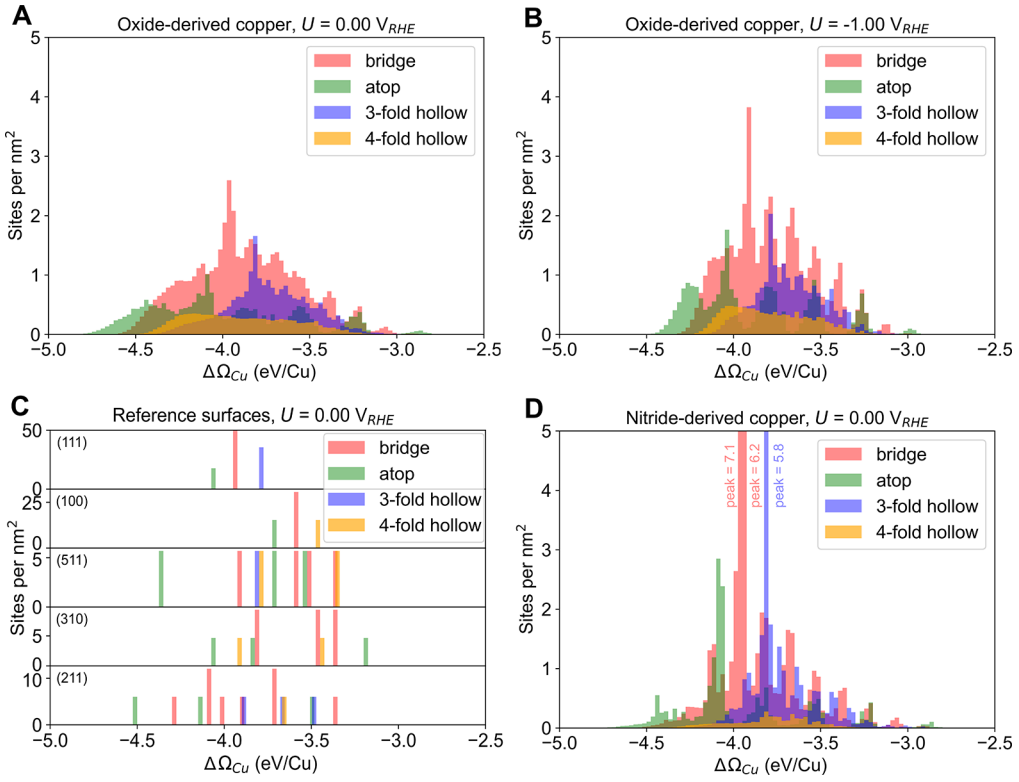

Figure 2. Distributions of constant potential copper binding energies, $\Delta\Omega_{Cu}$, on OD-Cu at 0.0 V vs RHE (a), $\Delta\Omega_{Cu}$ on OD-Cu at −1.0 V vs RHE (b), $\Delta\Omega_{Cu}$ on reference single crystal surfaces at 0.0 V vs RHE (c), and $\Delta\Omega_{Cu}$ on nitride derived Cu at 0.0 V vs RHE (d). See Figure S17 of the Supporting Information for representative site motifs on ideal surfaces.

functional[56] to describe exchange−correlation interactions. It should be noted that the important effect of surface strain is not captured by the α parameter scheme and is a topic of ongoing work. We built upon the previously published α parameter approach by incorporating the role of aqueous electrolyte and the applied potential in the α parameter model. The electrolyte and bias were captured by computing the training $\Delta\Omega_{Cu}$ systems at constant potential using the grand canonical potential approach described previously.[64] In brief, we compute the grand canonical potential,

$$\Omega = E - q\Phi \tag{1}$$

where E is the total electronic energy from DFT, q is the net charge of the system, and Φ is the Fermi level of the system. The charge in each state was optimized such that the system potential remains constant, and the effect of finite cell height was corrected.[65] We found that $\Delta\Omega_{Cu}$ can be approximated as a linear function of potential, reflecting the constant capacitance between states, thereby allowing us to incorporate the role of potential with a simple linear model adjusting the α parameters. Further details on the implementation of this model can be found in SI Notes 8 and 9. With this scheme we are able to compute $\Delta\Omega_{Cu}$ as a function of both the surface geometry in aqueous environment and the applied potential, illustrated in Figure 2.

In Figure 2 (a) and (b), we show the distribution of $\Delta\Omega_{Cu}$ on OD-Cu at a potential of 0.0 V vs RHE and −1.0 V vs RHE, respectively. Each surface site is classified according to the coordination of the binding atom, with a 1-fold coordination being classified as an "atop" site, 2-fold coordination being classified as a "bridge" site, and 3- and 4-fold coordination being classified as the respective "hollow" sites. Lowering the applied potential from 0.0 to −1.0 V vs RHE results in a contraction of the distribution of $\Delta\Omega_{Cu}$, with strong binding sites becoming weaker binding and weak binding sites becoming stronger binding. This can be understood from the perspective of a field-dipole model of adsorption: sites where Cu binds more weakly are undercoordinated (CN < 9), leading to a positive dipole moment between the surface and adsorbing Cu atom, which is stabilized by the electric field under an applied bias. Similarly, stronger binding sites are overcoordinated, resulting in a negative dipole moment which is destabilized by the field.

Strong peaks corresponding to (111) type sites can be seen at both potentials, with Figure 2 (c) showing the binding energies of common single crystal facets. The distribution of $\Delta\Omega_{Cu}$ on surfaces derived from cuprous sulfide and phosphide are very similar to the distribution found on OD-Cu, and can be found in SI Note 11, Figure S15. Figure 2 (d) shows the distribution for a Cu surface derived from Cu_3N (ND-Cu), which exhibits a stronger preference for (111) type sites. We attribute this to Cu (111) being the most stable facet (lowest surface energy; see SI Figure S4), and the initial geometry before Langevin quenching being very open and high in energy. Despite the higher prevalence of (111) type sites, which are typically not as selective toward C_{2+} products,[66] the distribution is otherwise comparable in width and features to that of OD-Cu. This was found to be the case for all heteroatom types tested, though structures in which the heteroatom consists of a significantly higher volume fraction of the initial structure may result in a different distribution. We note here that the effect of potential, although important to the relative surface energy of Cu, is by construction not incorporated in the EMT optimization. The possibility of

https://doi.org/10.1021/acsenergylett.1c01485
ACS Energy Lett. 2021, 6, 3252−3260

training the EMT model to capture the variation of surface energy with potential will be a topic of future study. Importantly, we find that Cu (111) remains the most stable surface facet at potentials less reducing than about −1.5 V vs RHE at pH 7 (see SI Note 5 and Figure S7 for more details).

Similar binding energy distributions across a wide variety of starting materials suggests that the manner in which the surface is roughened does not ultimately affect the type of sites catalytically available, though the finer details of the distribution can be affected as evidenced by ND-Cu. We note that the distribution of sites reaches a much wider range of binding energies than any of the single crystal facets. The narrow range of sites accessible from small, periodic simulation cells highlights both the challenges associated with modeling surfaces with little long-range order and the importance of careful single crystal experiments for comparison to theory.

We then developed scaling relations that map $\Delta\Omega_{Cu}$ directly to the binding energy, $\Delta\Omega_{ads}$, of relevant intermediates for CO2RR. We computed the constant potential binding energy of six intermediates important in determining activity toward CO2RR (CO*, OCCHO*, OCCOH*, CCO*, C*, OH*) on several single crystal facets (100, 111, 211, 310, 511, 533), using all site types available for each facet. Figure 3 shows the

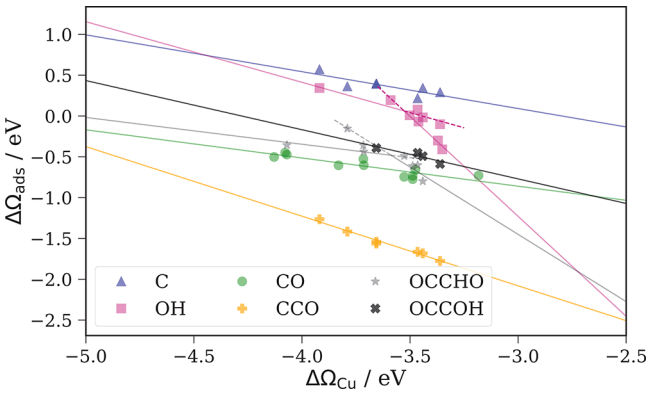

Figure 3. Scaling relations used to map the constant potential copper binding energy, $\Delta\Omega_{Cu}$, to constant potential binding energies for various bound intermediates important for CO2RR activity and selectivity, $\Delta\Omega_{ads}$. Lines shown are for the most stable site type for each adsorbate. C and CCO favor the 4-fold hollow, CO favors the on-top site, OCCOH prefers to be 2-fold coordinated across a bridge site, OH prefers the bridge in highly coordinated sites and the 4-fold hollow in undercoordinated sites, and OCCHO prefers to sit on-top on highly coordinated sites but shifts to laying flat across a 4-fold hollow on undercoordinated sites. See SI note 6 for scaling relations for all adsorbates and all site types.

scaling relations for the six intermediates binding to their respective most stable site type (atop, bridge, or 3- or 4-fold hollow) at an applied potential of 0.0 V vs RHE. We deliberately chose a wide span for the *x*-axis in this figure to match the *x*-axis of Figure 2, highlighting the lack of site types available despite a wide variety of single crystal surfaces tested.

As we describe in more detail below, the distributions of $\Delta\Omega_{C*}$, $\Delta\Omega_{CO*}$, and $\Delta\Omega_{OH*}$ were used in conjunction with previously published thermodynamic models of selectivity.[31,32] We note that we did not include OCCO* as it spontaneously decomposes into two adsorbed CO molecules at less reducing conditions, though it likely plays a role in the pathway to C_{2+} products.[30,32] Despite each scaling line consisting of points across a variety of surface facets, we find the mean absolute error to be smaller than 0.1 eV in all cases. Breaks occur in the scaling lines for OH* and OCCHO* as the most stable site type changes. In the case of OH*, the adsorbate prefers 4-fold hollow type sites on higher coordination (more negative $\Delta\Omega_{Cu}$) sites and bridge sites on lower coordination (more positive $\Delta\Omega_{Cu}$) sites. OCCHO* prefers an on-top configuration on higher coordination sites, such as on Cu (100) but prefers to lay flat across a 4-fold hollow site on lower coordination sites, such as the step of Cu (511). We note that at a given atom ensemble (surface site), the scaling line associated with the given surface site is evaluated rather than the most stable site. Further details of our analysis can be found in SI Note 6. We also remark that similar breaks may occur for other adsorbates outside the range of sites accessible by the facets tested here.

The negative slope for all scaling lines is indicative of the reversal in the trend of binding strength as a function of surface coordination when moving from Cu to the CO2RR adsorbates. The reversal is caused by Cu preferring a very high (12-fold) coordination, while most adsorbates prefer much lower coordination. Cu is therefore stronger binding on more coordinated surfaces, while the adsorbates tested here prefer at most 4-fold coordination (C), leading to stronger binding on undercoordinated sites (i.e., those with more positive $\Delta\Omega_{Cu}$). The magnitude of the slope of the scaling line controls the width of the distribution of adsorbate binding energies on the given facet, meaning the most stable site of CO* has a relatively narrow distribution (slope close to zero), while the most stable site of CCO* has a wider distribution. The scaling lines shown in Figure 3 are only for the most stable site types. In Figure 4 (a) we show the distribution of adsorbate binding energies for all site types, with scaling lines shown in SI Note 6, Figures S8−S13, and Table S1. In particular, the *C binding energies are bimodal due to the split between the 4-fold hollow configuration and the substantially less stable 3-fold hollow configuration.

We note that in order to determine the most favorable adsorption site given a certain surface motif (i.e., a surface atom ensemble) and a given adsorbate, each available site including atop, bridge, or hollow must be tested using the scaling lines for the site type and the $\Delta\Omega_{Cu}$ for the investigated site. This is described in SI note 6.

Overall the adsorbate binding energy distributions are far narrower than the Cu binding energy distribution, since the scaling lines seen in Figure 3 have slopes close to zero. More negative slopes, for instance as found with the scaling for *OH, lead to wider distributions. A shift in the preferred site leads to the distribution for *OCCHO being significantly wider, as the adsorbate prefers to lie flat across a 4-fold hollow at less coordinated sites. Among the adsorbates with two carbons tested here, we find *CCO to be the most thermodynamically stable intermediate, though formation barriers will ultimately determine the most important intermediate and are not determined in this study. Interestingly, more narrow distributions for some adsorbates suggests that the single crystal model typically used with computational studies is a better approximation than the Cu binding energy distribution alone would suggest.

Panels (c) and (d) of Figure 4 illustrate thermodynamic selectivity maps based on recent work from Tang et al.[31] at an applied potential of −0.7 and −1.1 V vs RHE, respectively. Here, the purple regions (denoted CH_4/C_{1+}) illustrate sites

https://doi.org/10.1021/acsenergylett.1c01485
ACS Energy Lett. 2021, 6, 3252−3260

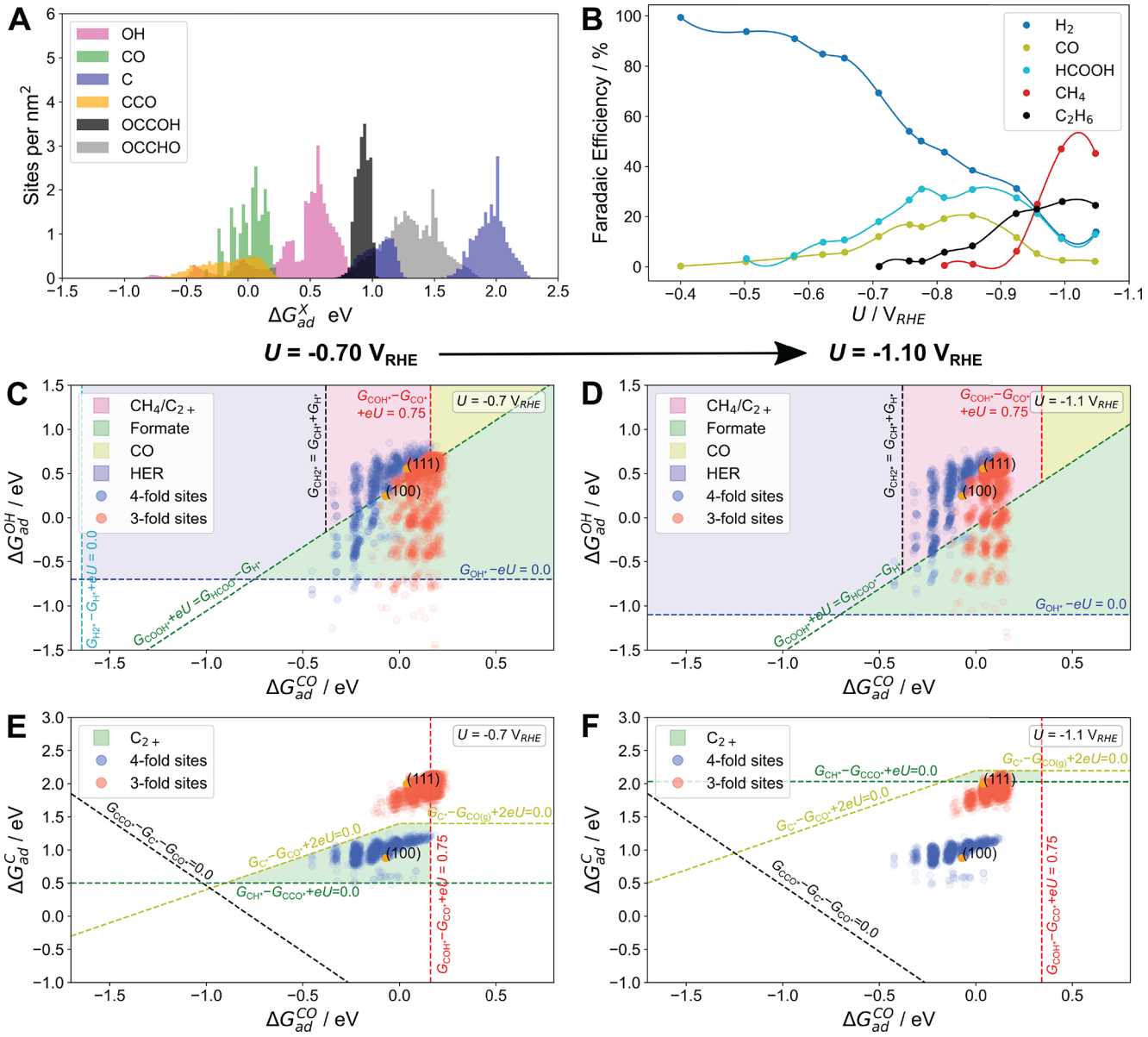

Figure 4. Distribution of constant potential binding free energies for CO2RR intermediates at an applied potential of $U = -0.7$ V vs RHE (a). Experimental[67] Faradaic efficiencies toward reduced products in CO2RR on polycrystalline copper (b). C_{1+} product selectivity plots defining regions of selectivity toward formate, HER and CO generation at an applied potential of $U = -0.7$ V vs RHE (c), and $U = -1.1$ V vs RHE (d). Here the selectivity regions are defined by the ΔG_{CO^*} and ΔG_{OH^*} descriptors based on Tang et al.[31] In panels (e) and (f), C_{2+} selectivity defined by the ΔG_{CO^*} and ΔG_{C^*} descriptors based on the work of Peng et al.[32] at applied potentials of $U = -0.7$ and -1.1 V vs RHE, respectively.

where it is thermodynamically favorable for adsorbed CO on the surface to undergo further reduction either to methane or potentially C_{2+} products. We note that a prerequisite for further reduction in this model is the ability to form *C, which precludes most 3-fold sites as seen in Figure 4 (a), and furthermore note that our model neglects the important role transport can play in selectivity[16,68,69] and is therefore only applicable in regions far from transport limitations.

The preference for formation of C_{2+} products rather than methane is illustrated in panels (e) and (f) of Figure 4, based on published work from Peng et al.[32] Here, we see most 4-fold hollow sites on roughened Cu prefer forming C−C bonds at potentials near where ethylene is observed experimentally, with data from Hori[67] on polycrystalline copper reproduced in panel (b). The model predicts the Faradaic efficiency toward methane to dominate at higher overpotentials, and with it a decline in preference to C_{2+} products, which is also supported by the experimental data. It is likely that a more roughened surface as found in some experiments,[55] with roughness factors more than 10 times that tested here, would exhibit a broader distribution that remains selective toward C_{2+} products over a wider potential range. We have estimated the roughness of our surface to be approximately 1.05 by computing the total number of surface sites and dividing the number of sites on a comparable (111) single crystal, which represents roughly a lower bound of the true roughness and is possibly not comparable to experimental roughness factors measured by capacitances relative to a reference value. A better experimental analog may be surface roughness as measured by atomic force microscopy, but this would be difficult to perform in an

https://doi.org/10.1021/acsenergylett.1c01485
ACS Energy Lett. 2021, 6, 3252−3260

electrolytic environment, and ex-situ measurements may convolute the roughness by oxidation in the air. Indeed the experiments on highly roughened copper show a growing Faradaic efficiency to C_{2+} products as the potential becomes more reducing than −0.7 V vs RHE, in contrast to the data from Hori on mechanically and electropolished polycrystalline copper. We hypothesize that a more roughened surface that captures mesoscale features such as porosity may bridge the 3-fold and 4-fold hollow site distributions for the binding energy of atomic carbon, leading to a greater number of sites active toward C_{2+} products in Figure 4 (e) and (f). Within our framework, a higher roughness could be achieved by using roughened oxide surface as our starting structure (as opposed to a single crystal oxide), randomly removing surface atoms to simulate ion bombardment, or randomizing the position of surface atoms before geometry optimization. These strategies will be a topic of future investigation. While the strategy we present in this work results in a relatively smooth surface compared to some experimental reports, it represents an important step forward in understanding surface roughness.

Experimentally, it has been found that roughening inhibits the appearance of CO in the gas phase, leading to enhanced selectivity (but not current density) to C_{2+} products.[24,70] This was explained with a simple model of a roughened surface, which was found to on average bind CO more strongly than single crystal Cu (100). Our results illustrate a similar but slightly different picture. Roughening does produce sites that bind CO stronger than low index single crystal Cu, but it also produces sites that bind CO more weakly, with Cu (100) being close to the arithmetic mean of the distribution of CO binding energies. Importantly though, the 4-fold sites that bind CO more weakly than Cu (100) also bind *OH more weakly, preventing the pathway to formate from being more thermodynamically feasible than the C_{1+} pathway. We note here that it is unlikely that *OH actually binds to roughened Cu under CO2RR conditions, as it would have a very strong driving force to reduce to water; rather, $\Delta\Omega_{OH}$ serves as a descriptor for the formation of formate. Competition between formate and the C_{1+} pathway highlight the success of tandem catalysis:[71−77] by utilizing a catalyst such as Ag which selectively reduces CO_2 to CO which then diffuses to Cu, the formate pathway is partially eliminated.

Many of the sites that bind *CO more strongly than Cu (100) are actually predicted to form formate, leading to a potential new design principle for Cu sites that are active for production of C_{2+} products. Our model suggests that while most 4-fold hollow sites are active toward reduction beyond CO, strongly undercoordinated 4-fold hollow sites will bind *OH too strongly and prefer the formation of formate. Instead, 4-fold hollow sites with higher coordination than Cu (100) are predicted to be more active to reduction beyond CO. Such a site can be found for instance in the 4-fold hollow site on Cu (310) below the step, though this type of site is not easily captured by a single crystal model. Highly coordinated 4-fold sites were also suggested to be active by a previous AIMD investigation into OD-Cu.[46] An alternative strategy to enhancing representation of overcoordinated 4-fold hollow sites might be by blocking the undercoordinated sites through, e.g., Au or Pb underdeposition.[78]

In conclusion, we have investigated four types of roughened Cu surfaces, each consisting of 10^6-10^7 atoms, with approximately 10 times fewer surface sites, and at a scale of 100 nm with accuracy comparable to GGA-DFT. Each site was categorized into one of four site types: atop, bridge, 3-fold hollow, 4-fold hollow. We computed constant potential Cu binding energies for each site using a local coordination environment, benchmarked against GGA-DFT with very low error. We then developed scaling relations to map these Cu binding energies to adsorbates relevant for CO2RR, which were fed into simple thermodynamic models of selectivity to determine the role of roughening in enhancing selectivity to C_{2+} products.

We find that single crystal models are insufficient to capture the wide range of sites found on electrochemically roughened Cu, with none of the facets tested coming close to matching the width of the distribution of Cu binding energies found on, e.g., OD-Cu. The distributions of individual adsorbate binding energies were found to be much narrower but still far from the single crystal approximation. The manner of surface roughening was found to not significantly affect the width of the distribution of Cu binding energies, though we found nitride derived Cu to have a higher representation of (111) type sites. Electrochemically roughened Cu surfaces such as OD-Cu produce a diverse mix of 3-fold and 4-fold hollow sites, with Cu (100) being near the arithmetic mean of the $\Delta\Omega_{CO}$ distribution, indicating the creation of both stronger and weaker binding sites. In support of previous experimental and theoretical literature, our model finds that square 4-fold sites are the most likely to be active toward C_{2+} products, though interestingly we find that the overcoordinated 4-fold hollow sites are the most likely to be active as undercoordinated hollows are found to prefer formation of formate. Avoiding the competition with formate through tandem catalysis has been demonstrated previously in the literature.

As a design principle our findings suggest enhancing the representation of overcoordinated 4-fold hollow sites will lead to improved selectivity to C_{2+} products and can be achieved in one of two ways. First, the direct synthesis of a single crystal facet which has overcoordinated 4-fold hollow sites as found on Cu (511) or (310). However, likely surface reconstruction as a result of applied bias, adsorbates, corrosion, or elevated Cu mobility at room temperature will complicate experimental realization of this strategy. Second, the blocking of undercoordinated sites through, e.g., Ag or Pb underdeposition as was done to demonstrate the activity of step sites in dissociating N_2 on Ru (0001).[78] Clearly our proposed model is an approximation, neglecting the important effects of strain, transport, potential dependent surface energies, active site dependent activation barriers, and mesoscale features such as porosity and grains. Nevertheless it represents a significant step forward in understanding how roughening enhances selectivity to C_{2+} products during CO2RR on Cu.

■ ASSOCIATED CONTENT

Supporting Information

The Supporting Information is available free of charge at https://pubs.acs.org/doi/10.1021/acsenergylett.1c01485.

Computational details; benchmarking of effective medium theory against GGA-DFT with figures of parity lines, nudged elastic bands, surface energies; benchmarking model surface thickness with a figure of convergence of local CN surface fraction; facile reduction to metallic Cu with a figure of thermodynamics and kinetics bar graph; potential dependence of surface energies with a figure of potential dependence of

https://doi.org/10.1021/acsenergylett.1c01485
ACS Energy Lett. 2021, 6, 3252−3260

surface energies; scaling lines for all site types and adsorbates with figures of the scaling lines and a table of slopes and intercepts for the scaling lines; overview over the parameter scheme; training set and tting procedure for the parameters with a table of the training set; adsorbate-site stability scaling relations with tables of adsorption sites and binding energies, fitted linear equations, α parameters, and coordination matrices; selectivity plots with a figure of scaling lines and a table of free energies; copper site stability distribution with a table of free energies and figures of site binding energy distributions, potential dependence of adsorption energy, and surface site motifs (PDF)

AUTHOR INFORMATION

Corresponding Authors

Frank Abild-Pedersen − *SUNCAT Center for Interface Science and Catalysis, SLAC National Accelerator Laboratory, Menlo Park, California 94025, United States;* orcid.org/0000-0002-1911-074X; Email: abild@slac.stanford.edu

Martin Head-Gordon − *Chemical Sciences Division, Lawrence Berkeley National Laboratory, Berkeley, California 94720, United States; Kenneth S. Pitzer Center for Theoretical Chemistry, Department of Chemistry, University of California, Berkeley, California 94720, United States;* orcid.org/0000-0002-4309-6669; Email: mhg@cchem.berkeley.edu

Alexis T. Bell − *Chemical Sciences Division, Lawrence Berkeley National Laboratory, Berkeley, California 94720, United States; Department of Chemical and Biomolecular Engineering, University of California, Berkeley, California 94720, United States;* orcid.org/0000-0002-5738-4645; Email: alexbell@berkeley.edu

Authors

Joseph A. Gauthier − *Chemical Sciences Division, Lawrence Berkeley National Laboratory, Berkeley, California 94720, United States; Department of Chemical and Biomolecular Engineering, University of California, Berkeley, California 94720, United States;* orcid.org/0000-0001-9542-0988

Joakim Halldin Stenlid − *SUNCAT Center for Interface Science and Catalysis, SLAC National Accelerator Laboratory, Menlo Park, California 94025, United States; SUNCAT Center for Interface Science and Catalysis, Department of Chemical Engineering, Stanford University, Stanford, California 94305, United States;* orcid.org/0000-0003-3832-2331

Complete contact information is available at: https://pubs.acs.org/10.1021/acsenergylett.1c01485

Author Contributions

[⊥]J.A.G. and J.H.S. contributed equally to this work

Notes

The authors declare no competing financial interest.

Coordinates and energies for the optimized structures are available at Catalysis-hub.org[79] at https://www.catalysis-hub.org/publications/Gauthierrole2021 and Materials Cloud (https://doi.org/10.24435/materialscloud:3s-7w).

ACKNOWLEDGMENTS

We thank the U.S. Department of Energy, Office of Science, Office of Advanced Scientific Computing Research, Scientific Discovery through Advanced Computing (SciDAC) program for support. This research used resources of the National Energy Research Scientific Computing Center, a DOE Office of Science User Facility supported by the Office of Science of the U.S. Department of Energy under Contract No. DE-AC02-05CH11231, allocations m2997 and mp54. F.A.P. and J.H.S. gratefully acknowledge funding via the Liquid Sunlight Alliance, which is supported by the U.S. Department of Energy, Office of Science, Office of Basic Energy Sciences, Fuels from Sunlight Hub under Award Number DE-SC0021266, and the Knut and Alice Wallenberg foundation (grant no. 2019.0586), respectively. This research also used computing resources at the Molecular Graphics and Computation Facility operated by the College of Chemistry at the University of California, Berkeley, grant no. NIH S10OD023532. The authors also thank Jakob Schiøtz for helpful discussions when installing and running EMT as implemented in Asap3.

REFERENCES

(1) De Luna, P.; Hahn, C.; Higgins, D.; Jaffer, S. A.; Jaramillo, T. F.; Sargent, E. H. What would it take for renewably powered electrosynthesis to displace petrochemical processes? *Science* **2019**, *364*, No. eaav3506.

(2) Nitopi, S.; Bertheussen, E.; Scott, S. B.; Liu, X.; Engstfeld, A. K.; Horch, S.; Seger, B.; Stephens, I. E. L.; Chan, K.; Hahn, C.; Nørskov, J. K.; Jaramillo, T. F.; Chorkendorff, I. Progress and Perspectives of Electrochemical CO_2 Reduction on Copper in Aqueous Electrolyte. *Chem. Rev.* **2019**, *119*, 7610−7672.

(3) Jouny, M.; Luc, W.; Jiao, F. General techno-economic analysis of CO_2 electrolysis systems. *Ind. Eng. Chem. Res.* **2018**, *57*, 2165−2177.

(4) Spurgeon, J. M.; Kumar, B. A comparative technoeconomic analysis of pathways for commercial electrochemical CO_2 reduction to liquid products. *Energy Environ. Sci.* **2018**, *11*, 1536−1551.

(5) Ogura, K.; Yano, H.; Shirai, F. Catalytic reduction of CO_2 to ethylene by electrolysis at a three-phase interface. *J. Electrochem. Soc.* **2003**, *150*, D163.

(6) Yano, H.; Tanaka, T.; Nakayama, M.; Ogura, K. Selective electrochemical reduction of CO_2 to ethylene at a three-phase interface on copper (I) halide-confined Cu-mesh electrodes in acidic solutions of potassium halides. *J. Electroanal. Chem.* **2004**, *565*, 287−293.

(7) Burdyny, T.; Smith, W. A. CO_2 reduction on gas-diffusion electrodes and why catalytic performance must be assessed at commercially-relevant conditions. *Energy Environ. Sci.* **2019**, *12*, 1442−1453.

(8) Li, Y. C.; Zhou, D.; Yan, Z.; Goncalves, R. H.; Salvatore, D. A.; Berlinguette, C. P.; Mallouk, T. E. Electrolysis of CO_2 to syngas in bipolar membrane-based electrochemical cells. *ACS Energy Letters* **2016**, *1*, 1149−1153.

(9) Jhong, H.-R.; Brushett, F. R.; Kenis, P. J. The effects of catalyst layer deposition methodology on electrode performance. *Adv. Energy Mater.* **2013**, *3*, 589−599.

(10) Dufek, E. J.; Lister, T. E.; Stone, S. G.; McIlwain, M. E. Operation of a pressurized system for continuous reduction of CO_2. *J. Electrochem. Soc.* **2012**, *159*, F514.

(11) Weng, L.-C.; Bell, A. T.; Weber, A. Z. Towards membrane-electrode assembly systems for CO_2 reduction: a modeling study. *Energy Environ. Sci.* **2019**, *12*, 1950−1968.

(12) Paik, W.; Andersen, T.; Eyring, H. Kinetic studies of the electrolytic reduction of carbon dioxide on the mercury electrode. *Electrochim. Acta* **1969**, *14*, 1217−1232.

(13) Hori, Y.; Suzuki, S. Electrolytic reduction of carbon dioxide at mercury electrode in aqueous solution. *Bull. Chem. Soc. Jpn.* **1982**, *55*, 660−665.
(14) Resasco, J.; Chen, L. D.; Clark, E.; Tsai, C.; Hahn, C.; Jaramillo, T. F.; Chan, K.; Bell, A. T. Promoter effects of alkali metal cations on the electrochemical reduction of carbon dioxide. *J. Am. Chem. Soc.* **2017**, *139*, 11277−11287.
(15) Ringe, S.; Clark, E. L.; Resasco, J.; Walton, A.; Seger, B. J.; Bell, A. T.; Chan, K. Understanding Cation Effects in Electrochemical CO_2 Reduction. *Energy Environ. Sci.* **2019**, *12*, 3001−3014.
(16) Bui, J. C.; Kim, C.; Weber, A. Z.; Bell, A. T. Dynamic Boundary Layer Simulation of Pulsed CO_2 Electrolysis on a Copper Catalyst. *ACS Energy Letters* **2021**, *6*, 1181−1188.
(17) Kim, C.; Weng, L.-C.; Bell, A. T. Impact of Pulsed Electrochemical Reduction of CO_2 on the Formation of C_{2+} Products over Cu. *ACS Catal.* **2020**, *10*, 12403−12413.
(18) Oguma, T.; Azumi, K. Improvement of Electrochemical Reduction of CO_2 Using the Potential-Pulse Polarization Method. *Electrochemistry* **2020**, *88*, 451−456.
(19) Frese, K. W., Jr Electrochemical reduction of CO_2 at intentionally oxidized copper electrodes. *J. Electrochem. Soc.* **1991**, *138*, 3338.
(20) Kyriacou, G.; Anagnostopoulos, A. Electroreduction of CO2 on differently prepared copper electrodes: The influence of electrode treatment on the current efficiences. *J. Electroanal. Chem.* **1992**, *322*, 233−246.
(21) Momose, Y.; Sato, K.; Ohno, O. Electrochemical reduction of CO_2 at copper electrodes and its relationship to the metal surface characteristics. *Surf. Interface Anal.* **2002**, *34*, 615−618.
(22) Li, C. W.; Kanan, M. W. CO_2 reduction at low overpotential on Cu electrodes resulting from the reduction of thick Cu_2O films. *J. Am. Chem. Soc.* **2012**, *134*, 7231−7234.
(23) Li, C. W.; Ciston, J.; Kanan, M. W. Electroreduction of carbon monoxide to liquid fuel on oxide-derived nanocrystalline copper. *Nature* **2014**, *508*, 504−507.
(24) Jiang, K.; Huang, Y.; Zeng, G.; Toma, F. M.; Goddard, W. A., III; Bell, A. T. Effects of surface roughness on the electrochemical reduction of CO_2 over Cu. *ACS Energy Letters* **2020**, *5*, 1206−1214.
(25) Hori, Y.; Takahashi, I.; Koga, O.; Hoshi, N. Selective formation of C_2 compounds from electrochemical reduction of CO_2 at a series of copper single crystal electrodes. *J. Phys. Chem. B* **2002**, *106*, 15−17.
(26) Hori, Y.; Takahashi, I.; Koga, O.; Hoshi, N. Electrochemical reduction of carbon dioxide at various series of copper single crystal electrodes. *J. Mol. Catal. A: Chem.* **2003**, *199*, 39−47.
(27) Bagger, A.; Ju, W.; Varela, A. S.; Strasser, P.; Rossmeisl, J. Electrochemical CO_2 reduction: classifying Cu facets. *ACS Catal.* **2019**, *9*, 7894−7899.
(28) Huang, Y.; Handoko, A. D.; Hirunsit, P.; Yeo, B. S. Electrochemical reduction of CO_2 using copper single-crystal surfaces: effects of CO* coverage on the selective formation of ethylene. *ACS Catal.* **2017**, *7*, 1749−1756.
(29) Montoya, J. H.; Shi, C.; Chan, K.; Nørskov, J. K. Theoretical insights into a CO dimerization mechanism in CO_2 electroreduction. *J. Phys. Chem. Lett.* **2015**, *6*, 2032−2037.
(30) Garza, A. J.; Bell, A. T.; Head-Gordon, M. Mechanism of CO_2 reduction at copper surfaces: pathways to C_2 products. *ACS Catal.* **2018**, *8*, 1490−1499.
(31) Tang, M. T.; Peng, H.; Lamoureux, P. S.; Bajdich, M.; Abild-Pedersen, F. From electricity to fuels: descriptors for C_1 selectivity in electrochemical CO_2 reduction. *Appl. Catal., B* **2020**, *279*, 119384.
(32) Peng, H.; Tang, M. T.; Liu, X.; Lamoureux, P. S.; Bajdich, M.; Abild-Pedersen, F. The role of atomic carbon in directing electrochemical $CO_{(2)}$ reduction to multicarbon products. *Energy Environ. Sci.* **2021**, *14*, 473−482.
(33) Arán-Ais, R. M.; Scholten, F.; Kunze, S.; Rizo, R.; Cuenya, B. R. The role of in situ generated morphological motifs and Cu (i) species in C 2+ product selectivity during CO_2 pulsed electroreduction. *Nature Energy* **2020**, *5*, 317−325.
(34) Velasco-Velez, J.-J.; Jones, T.; Gao, D.; Carbonio, E.; Arrigo, R.; Hsu, C.-J.; Huang, Y.- C.; Dong, C.-L.; Chen, J.-M.; Lee, J.-F.; et al. The role of the copper oxidation state in the electrocatalytic reduction of CO_2 into valuable hydrocarbons. *ACS Sustainable Chem. Eng.* **2019**, *7*, 1485−1492.
(35) Möller, T.; Scholten, F.; Thanh, T. N.; Sinev, I.; Timoshenko, J.; Wang, X.; Jovanov, Z.; Gliech, M.; Roldan Cuenya, B.; Varela, A. S.; et al. Electrocatalytic CO_2Reduction on CuO_x Nanocubes: Tracking the Evolution of Chemical State, Geometric Structure, and Catalytic Selectivity using Operando Spectroscopy. *Angew. Chem.* **2020**, *132*, 18130−18139.
(36) Lum, Y.; Ager, J. W. Stability of residual oxides in oxide-derived copper catalysts for electrochemical CO_2 reduction investigated with ^{18}O labeling. *Angew. Chem., Int. Ed.* **2018**, *57*, 551−554.
(37) Eilert, A.; Cavalca, F.; Roberts, F. S.; Osterwalder, J.; Liu, C.; Favaro, M.; Crumlin, E. J.; Ogasawara, H.; Friebel, D.; Pettersson, L. G.; et al. Subsurface oxygen in oxide-derived copper electrocatalysts for carbon dioxide reduction. *J. Phys. Chem. Lett.* **2017**, *8*, 285−290.
(38) Verdaguer-Casadevall, A.; Li, C. W.; Johansson, T. P.; Scott, S. B.; McKeown, J. T.; Kumar, M.; Stephens, I. E.; Kanan, M. W.; Chorkendorff, I. Probing the active surface sites for CO reduction on oxide-derived copper electrocatalysts. *J. Am. Chem. Soc.* **2015**, *137*, 9808−9811.
(39) Cheng, D.; Zhao, Z.-J.; Zhang, G.; Yang, P.; Li, L.; Gao, H.; Liu, S.; Chang, X.; Chen, S.; Wang, T.; et al. The nature of active sites for carbon dioxide electroreduction over oxide-derived copper catalysts. *Nat. Commun.* **2021**, *12*, 395.
(40) Liu, C.; Lourenço, M. P.; Hedstrom, S.; Cavalca, F.; Diaz-Morales, O.; Duarte, H. A.; Nilsson, A.; Pettersson, L. G. Stability and effects of subsurface oxygen in oxide-derived Cu catalyst for CO_2 reduction. *J. Phys. Chem. C* **2017**, *121*, 25010−25017.
(41) Melander, M. M.; Kuisma, M. J.; Christensen, T. E. K.; Honkala, K. Grand-canonical approach to density functional theory of electrocatalytic systems: Thermodynamics of solid-liquid interfaces at constant ion and electrode potentials. *J. Chem. Phys.* **2019**, *150*, 041706.
(42) Schwarz, K.; Sundararaman, R. The electrochemical interface in first-principles calculations. *Surf. Sci. Rep.* **2020**, *75*, 100492.
(43) Liu, X.; Xiao, J.; Peng, H.; Hong, X.; Chan, K.; Nørskov, J. K. Understanding trends in electrochemical carbon dioxide reduction rates. *Nat. Commun.* **2017**, *8*, 15438.
(44) Ting, L. R. L.; García-Muelas, R.; Martín, A. J.; Veenstra, F. L.; Chen, S. T.-J.; Peng, Y.; Per, E. Y. X.; Pablo-García, S.; López, N.; Pérez-Ramírez, J.; et al. Electrochemical Reduction of Carbon Dioxide to 1-Butanol on Oxide-Derived Copper. *Angew. Chem.* **2020**, *132*, 21258−21265.
(45) Choi, C.; Kwon, S.; Cheng, T.; Xu, M.; Tieu, P.; Lee, C.; Cai, J.; Lee, H. M.; Pan, X.; Duan, X.; et al. Highly active and stable stepped Cu surface for enhanced electrochemical CO_2 reduction to C_2H_4. *Nature Catalysis* **2020**, *3*, 804−812.
(46) Dattila, F.; Garcıa-Muelas, R.; Lopez, N. Active and Selective Ensembles in Oxide-Derived Copper Catalysts for CO_2 Reduction. *ACS Energy Letters* **2020**, *5*, 3176−3184.
(47) Chen, Y.; Huang, Y.; Cheng, T.; Goddard, W. A., III Identifying active sites for CO_2 reduction on dealloyed gold surfaces by combining machine learning with multiscale simulations. *J. Am. Chem. Soc.* **2019**, *141*, 11651−11657.
(48) Velasco-Velez, J.-J.; Mom, R. V.; Sandoval-Diaz, L.-E.; Falling, L. J.; Chuang, C.-H.; Gao, D.; Jones, T. E.; Zhu, Q.; Arrigo, R.; Roldan Cuenya, B.; et al. Revealing the active phase of copper during the electroreduction of CO_2 in aqueous electrolyte by correlating in situ X-ray spectroscopy and in situ electron microscopy. *ACS Energy Letters* **2020**, *5*, 2106−2111.
(49) Garza, A. J.; Bell, A. T.; Head-Gordon, M. Is subsurface oxygen necessary for the electrochemical reduction of CO_2 on copper? *J. Phys. Chem. Lett.* **2018**, *9*, 601−606.
(50) Fields, M.; Hong, X.; Nørskov, J. K.; Chan, K. Role of subsurface oxygen on Cu surfaces for CO2 electrochemical reduction. *J. Phys. Chem. C* **2018**, *122*, 16209−16215.

https://doi.org/10.1021/acsenergylett.1c01485
ACS Energy Lett. 2021, 6, 3252−3260

(51) Jacobsen, K.; Norskov, J.; Puska, M. J. Interatomic interactions in the effective-medium theory. *Phys. Rev. B: Condens. Matter Mater. Phys.* **1987**, *35*, 7423.
(52) Jacobsen, K. W. Bonding in metallic systems, an effective medium approach. *Ph.D. thesis*, Physics Laboratory, HC Ørsted Institute, University of Copenhagen, 1987.
(53) Jacobsen, K. W.; Stoltze, P.; Nørskov, J. A semi-empirical effective medium theory for metals and alloys. *Surf. Sci.* **1996**, *366*, 394−402.
(54) Larsen, A. H.; Mortensen, J. J.; Blomqvist, J.; Castelli, I. E.; Christensen, R.; Du lak, M.; Friis, J.; Groves, M. N.; Hammer, B.; Hargus, C.; et al. The atomic simulation environment—a Python library for working with atoms. *J. Phys.: Condens. Matter* **2017**, *29*, 273002.
(55) Ebaid, M.; Jiang, K.; Zhang, Z.; Drisdell, W. S.; Bell, A. T.; Cooper, J. K. Production of C_2/C_3 oxygenates from planar copper nitride-derived mesoporous copper via electrochemical reduction of CO_2. *Chem. Mater.* **2020**, *32*, 3304−3311.
(56) Hammer, B.; Hansen, L. B.; Nørskov, J. K. Improved adsorption energetics within density-functional theory using revised Perdew-Burke-Ernzerhof functionals. *Phys. Rev. B: Condens. Matter Mater. Phys.* **1999**, *59*, 7413.
(57) Kresse, G.; Hafner, J. Ab initio molecular dynamics for liquid metals. *Phys. Rev. B: Condens. Matter Mater. Phys.* **1993**, *47*, 558.
(58) Kresse, G.; Furthmüller, J. Efficiency of ab-initio total energy calculations for metals and semiconductors using a plane-wave basis set. *Comput. Mater. Sci.* **1996**, *6*, 15−50.
(59) Kresse, G.; Furthmüller, J. Efficient iterative schemes for ab initio total-energy calculations using a plane-wave basis set. *Phys. Rev. B: Condens. Matter Mater. Phys.* **1996**, *54*, 11169.
(60) Roling, L. T.; Li, L.; Abild-Pedersen, F. Configurational Energies of Nanoparticles Based on Metal−Metal Coordination. *J. Phys. Chem. C* **2017**, *121*, 23002−23010.
(61) Choksi, T. S.; Roling, L. T.; Streibel, V.; Abild-Pedersen, F. Predicting adsorption properties of catalytic descriptors on bimetallic nanoalloys with site-specific precision. *J. Phys. Chem. Lett.* **2019**, *10*, 1852−1859.
(62) Roling, L. T.; Choksi, T. S.; Abild-Pedersen, F. A coordination-based model for transition metal alloy nanoparticles. *Nanoscale* **2019**, *11*, 4438−4452.
(63) Roling, L. T.; Abild-Pedersen, F. Structure-Sensitive Scaling Relations: Adsorption Energies from Surface Site Stability. *ChemCatChem* **2018**, *10*, 1643−1650.
(64) Goodpaster, J. D.; Bell, A. T.; Head-Gordon, M. Identification of possible pathways for C−C bond formation during electrochemical reduction of CO_2: New theoretical insights from an improved electrochemical model. *J. Phys. Chem. Lett.* **2016**, *7*, 1471−1477.
(65) Gauthier, J. A.; Dickens, C. F.; Ringe, S.; Chan, K. Practical considerations for continuum models applied to surface electrochemistry. *ChemPhysChem* **2019**, *20*, 3074−3080.
(66) Hahn, C.; Hatsukade, T.; Kim, Y.-G.; Vailionis, A.; Baricuatro, J. H.; Higgins, D. C.; Nitopi, S. A.; Soriaga, M. P.; Jaramillo, T. F. Engineering Cu surfaces for the electrocatalytic conversion of CO_2: Controlling selectivity toward oxygenates and hydrocarbons. *Proc. Natl. Acad. Sci. U. S. A.* **2017**, *114*, 5918−5923.
(67) Hori, Y.; Murata, A.; Takahashi, R. Formation of hydrocarbons in the electrochemical reduction of carbon dioxide at a copper electrode in aqueous solution. *J. Chem. Soc., Faraday Trans. 1* **1989**, *85*, 2309−2326.
(68) Nguyen, D. L. T.; Lee, C. W.; Na, J.; Kim, M.-C.; Tu, N. D. K.; Lee, S. Y.; Sa, Y. J.; Won, D. H.; Oh, H.-S.; Kim, H.; et al. Mass transport control by surface graphene oxide for selective CO production from electrochemical CO_2 reduction. *ACS Catal.* **2020**, *10*, 3222−3231.
(69) Singh, M. R.; Goodpaster, J. D.; Weber, A. Z.; Head-Gordon, M.; Bell, A. T. Mechanistic insights into electrochemical reduction of CO2 over Ag using density functional theory and transport models. *Proc. Natl. Acad. Sci. U. S. A.* **2017**, *114*, E8812−E8821.
(70) Heenen, H. H.; Kastlunger, G.; Shin, H.; Overa, S.; Gauthier, J. A.; Jiao, F.; Chan, K. Mechanism for acetate formation in $CO_{(2)}$ reduction on Cu: Selectivity trends with pH and nanostructuring derive from mass transport. *ChemRxiv* **2021**, DOI: 10.33774/chemrxiv-2021-p3d4s (accessed June 28, 2021).
(71) Morales-Guio, C. G.; Cave, E. R.; Nitopi, S. A.; Feaster, J. T.; Wang, L.; Kuhl, K. P.; Jackson, A.; Johnson, N. C.; Abram, D. N.; Hatsukade, T.; et al. Improved CO_2 reduction activity towards C_{2+} alcohols on a tandem gold on copper electrocatalyst. *Nature Catalysis* **2018**, *1*, 764−771.
(72) Chen, C.; Li, Y.; Yu, S.; Louisia, S.; Jin, J.; Li, M.; Ross, M. B.; Yang, P. Cu-Ag Tandem Catalysts for High-Rate CO_2 Electrolysis toward Multicarbons. *Joule* **2020**, *4*, 1688−1699.
(73) Jia, H.; Yang, Y.; Chow, T. H.; Zhang, H.; Liu, X.; Wang, J.; Zhang, C.-y. Symmetry-Broken Au−Cu Heterostructures and their Tandem Catalysis Process in Electrochemical CO_2 Reduction. *Adv. Funct. Mater.* **2021**, *31*, 2101255.
(74) Lin, L.; Liu, T.; Xiao, J.; Li, H.; Wei, P.; Gao, D.; Nan, B.; Si, R.; Wang, G.; Bao, X. Enhancing CO_2 Electroreduction to Methane with a Cobalt Phthalocyanine and Zinc−Nitrogen−Carbon Tandem Catalyst. *Angew. Chem., Int. Ed.* **2020**, *59*, 22408−22413.
(75) Zhang, H.; Chang, X.; Chen, J. G.; Goddard, W. A.; Xu, B.; Cheng, M.-J.; Lu, Q. Computational and experimental demonstrations of one-pot tandem catalysis for electrochemical carbon dioxide reduction to methane. *Nat. Commun.* **2019**, *10*, 3340.
(76) Iyengar, P.; Kolb, M. J.; Pankhurst, J. R.; Calle-Vallejo, F.; Buonsanti, R. Elucidating the Facet-Dependent Selectivity for CO2 Electroreduction to Ethanol of Cu−Ag Tandem Catalysts. *ACS Catal.* **2021**, *11*, 4456−4463.
(77) Zhu, Y.; Cui, X.; Liu, H.; Guo, Z.; Dang, Y.; Fan, Z.; Zhang, Z.; Hu, W. Tandem catalysis in electrochemical CO_2 reduction reaction. *Nano Res.* **2021**, DOI: 10.1007/s12274-021-3448-2.
(78) Dahl, S.; Logadottir, A.; Egeberg, R.; Larsen, J.; Chorkendorff, I.; Törnqvist, E.; Nørskov, J. K. Role of steps in N_2 activation on Ru (0001). *Phys. Rev. Lett.* **1999**, *83*, 1814.
(79) Winther, K. T.; Hoffmann, M. J.; Boes, J. R.; Mamun, O.; Bajdich, M.; Bligaard, T. Catalysis-Hub.org, an open electronic structure database for surface reactions. *Sci. Data* **2019**, *6*, 75.

https://doi.org/10.1021/acsenergylett.1c01485
ACS Energy Lett. 2021, 6, 3252−3260